A lattice Boltzmann approach for modeling coupled evaporation/precipitation processes in porous media

Alexander Reinauer[1], Louis Oberer[1], Alexander Schlaich[2], and Christian Holm[1]

[1]Universitat Stuttgart Institut fur Computerphysik
[2]Technische Universität Hamburg Institut für Physik funktionaler Materialien

December 17, 2025

Abstract

We present a novel numerical approach for simulating coupled evaporation and salt precipitation processes in porous media using the lattice Boltzmann method. Our model combines a Shan-Chen multiphase flow framework with a volume-based discretization method for diffusing salt species, where the coupling mechanism operates through solvation energy differences. The framework incorporates a precipitation model based on first-order reaction kinetics, enabling the transformation of fluid cells into solid crystal cells upon reaching threshold concentrations. We verify our model against analytical solutions for crystal growth and evaporation rates, demonstrating excellent agreement. The model is then applied to investigate the influence of wetting properties on evaporation and salt precipitation in porous media. Our simulations reveal that the wettability of both the porous medium and the precipitated salt crystals has a significant impact on precipitation patterns and pore clogging. Notably, increased salt crystal wettability promotes more effective pore blocking, substantially reducing permeability and evaporation rates. We find that the slowest evaporation occurs when salt crystals have high wettability, while the porous medium exhibits lower wettability because this configuration maximizes pore clogging. This work presents a novel framework to gain insight into the intricate interplay between fluid dynamics, wetting properties, and salt precipitation in porous media, with implications for understanding soil salinization, building material degradation, and the formation of geological salt crusts.

A lattice Boltzmann approach for modeling coupled evaporation/precipitation processes in porous media

Alexander Reinauer[1], **Louis Oberer**[1], **Alexander Schlaich**[2], **Christian Holm**[1]

[1]Institute for Computational Physics, University of Stuttgart, 70569 Stuttgart, Germany
[2]Institute for Physics of Functional Materials, Hamburg University of Technology, 21073 Hamburg, Germany

Key Points:

- Novel coupled lattice Boltzmann model for evaporation induced precipitation with volume based solute transport model
- New interface-localized contact-angle scheme enabling robust wettability control
- Relative wettability of salt and matrix controls crystal growth, clogging, and evaporation decline

Corresponding author: Christian Holm, holm@icp.uni-stuttgart.de

Abstract

We present a novel numerical approach for simulating coupled evaporation and salt precipitation processes in porous media using the lattice Boltzmann method. Our model combines a Shan-Chen multiphase flow framework with a volume-based discretization method for diffusing salt species, where the coupling mechanism operates through solvation energy differences. The framework incorporates a precipitation model based on first-order reaction kinetics, enabling the transformation of fluid cells into solid crystal cells upon reaching threshold concentrations. We verify our model against analytical solutions for crystal growth and evaporation rates, demonstrating excellent agreement. The model is then applied to investigate the influence of wetting properties on evaporation and salt precipitation in porous media. Our simulations reveal that the wettability of both the porous medium and the precipitated salt crystals has a significant impact on precipitation patterns and pore clogging. Notably, increased salt crystal wettability promotes more effective pore blocking, substantially reducing permeability and evaporation rates. We find that the slowest evaporation occurs when salt crystals have high wettability, while the porous medium exhibits lower wettability because this configuration maximizes pore clogging. This work presents a novel framework to gain insight into the intricate interplay between fluid dynamics, wetting properties, and salt precipitation in porous media, with implications for understanding soil salinization, building material degradation, and the formation of geological salt crusts.

1 Introduction

Evaporation-induced precipitation in porous media is a ubiquitous pore-scale process in which phase change, solute transport, and mineral crystallization interact within a confined, heterogeneous geometry. It plays a crucial role in a broad range of natural and engineered systems, including soil fertility and salinization (Machado & Serralheiro, 2017; Lasser et al., 2020), particularly in arid and semi-arid regions (Singh, 2022), geological CO_2 sequestration where salt deposition can impair injectivity (He et al., 2022; Akindipe et al., 2021, 2022), and the durability of building materials where crystallization drives weathering and damage (Espinosa-Marzal & Scherer, 2010; Flatt et al., 2017). Despite its importance, predictive modeling remains challenging because the macroscopic response (e.g., evaporation rate decline, permeability loss, evolving saturation patterns) emerges from a complex interplay between water evaporation, solute advection-diffusion, salt nucleation, crystal growth, and changes in pore morphology (Nachshon & Weisbrod, 2015).

From a pore-scale perspective, evaporation establishes strong gradients in capillary pressure and vapor concentration, driving liquid redistribution through capillary flow and thin films while simultaneously concentrating dissolved species near phase boundaries. Once local supersaturation is reached, precipitation can occur at preferred nucleation sites and may progressively occlude flow pathways, thereby altering hydraulic connectivity and shifting the location of the active evaporation front. Capturing this feedback requires models that can resolve vapor-liquid interfacial dynamics and moving contact lines, capillary-driven multiphase flow including meniscus curvature and corner-film transport, and precipitation kinetics and the associated evolution of the pore space (Veran-Tissoires & Prat, 2014; Kharaghani, 2019; Shokri et al., 2024). These requirements motivate pore-scale modeling approaches that go beyond effective-medium descriptions and explicitly connect transport and reaction processes to the underlying microstructure.

Two complementary modeling paradigms have therefore been widely pursued. The first comprises direct numerical simulations (DNS), in which the pore geometry is explicitly resolved, and the coupled equations governing multiphase flow and mass transport are solved. DNS can capture mechanistic details ranging from interface curvature effects to heterogeneous nucleation at solid surfaces. Representative approaches include,

but are not restricted to, smoothed particle hydrodynamics (Tartakovsky et al., 2007), finite-element/finite-volume continuum methods (Veran-Tissoires & Prat, 2014; Rohde & Von Wolff, 2021), and lattice Boltzmann methods (LBM) (Yang et al., 2023). Among these, LBM is particularly attractive for multiphase flow in complex porous geometries due to its locality, straightforward handling of irregular boundaries, and natural parallel scalability (Liu et al., 2016). Several multiphase LBM formulations exist (Krüger et al., 2017), including the pseudopotential model (Shan & Chen, 1993), free-energy approaches (Swift et al., 1995, 1996), and color-gradient methods (Leclaire et al., 2017). Building on these developments, recent work has moved toward fully coupled descriptions of gas-liquid flow, solute transport, and salt precipitation (Chen et al., 2015; Yang et al., 2023), enabling pore-scale studies of how crystallization modifies flow paths and evaporation dynamics.

The second paradigm is provided by pore network models (PNM), which idealize the pore space as a network of pores connected by throats and simulate multiphase flow and transport using reduced-order physics informed by pore-scale geometry. PNMs are computationally efficient and thus well-suited for larger spatial and temporal scales, extensive parametric studies, and upscaling. Importantly, they can incorporate pore-size distributions, structural heterogeneity, and wettability transparently and directly relate these features to evaporation rates, saturation patterns, and preferential precipitation locations (Veran-Tissoires & Prat, 2014; Dashtian et al., 2018). A substantial body of work, including micro-model experiments and pore-network modeling over many years by Prat and co-workers, has established PNMs as a central tool to rationalize drying regimes, invasion patterns, and salt deposition pathways (e.g., related network-modeling studies and recent advances (Laurindo & Prat, 1996; Prat, 2007; Veran-Tissoires & Prat, 2014; Dashtian et al., 2018; Roy et al., 2022; Fei et al., 2024; Schollenberger et al., 2025)). At the same time, the reduced dimensionality of PNMs necessitates constitutive closures for interfacial dynamics, thin films, and precipitation-induced pore-space evolution, which are most reliably informed by DNS.

In this context, there is a continued need for pore-scale simulation frameworks that resolve the coupled gas-liquid dynamics during evaporation, treat multicomponent solute transport in a thermodynamically consistent and numerically stable manner, and include precipitation and the resulting microstructural evolution, while remaining flexible with respect to wettability and complex geometries. Here, we present a lattice Boltzmann approach for modeling coupled evaporation/precipitation processes in porous media. Our model is based on a well-established Shan-Chen extension for multiphase LBM (Chen et al., 2014), coupled to a volume-based solute transport scheme (Capuani et al., 2004; Rempfer et al., 2016) and a precipitation mechanism (Chen et al., 2013), including a novel contact-angle formulation that enables robust control of wettability. The resulting framework provides a comprehensive tool to investigate the fundamental mechanisms governing evaporation-induced precipitation, quantify its impact on evaporation rates, and analyze how salt deposition drives the evolution of pore structure.

2 Methodology

The model employed here consists of multiple phases (fluid and gas) which are needed to simulate the evaporation and precipitation processes together with a solid porous matrix phase. First, the treatment of hydrodynamics will be explained, captured using a lattice Boltzmann (LB) solver with a Shan-Chen (SC) extension to simulate multiphase flows. Next, an advection-diffusion solver is introduced which solves the advection and diffusion equations for a diffusive chemical species. The precipitation process of diffusive species is modeled with a surface reaction equation. Lastly, the coupling between the model components is introduced. The implementations of the following equations are carried out using the code generation packages pystencils (Bauer et al., 2019; Hennig et al., 2023) and lbmpy (Bauer et al., 2021).

2.1 Lattice Boltzmann

The discretized LB equation using a two-relaxation-time method is given as (Krüger et al., 2017)

$$f_i^* = f_i - \omega^+ \Delta t \left(f_i^+ - f_i^{eq,+}\right) - \omega^- \Delta t \left(f_i^- - f_i^{eq,-}\right) + S_i. \tag{1}$$

In contrast to the standard single-relaxation-time (SRT) Bhatnagar-Gross-Krook model, the populations are constructed in even and odd populations

$$f_i^+ = \tfrac{f_i + f_{\bar{i}}}{2} \tag{2a}$$
$$f_i^- = \tfrac{f_i - f_{\bar{i}}}{2}, \tag{2b}$$

where the bar represents the populations with symmetric velocities in the opposite direction. These moments are relaxed with two relaxation rates $\omega^{\pm}$. Here, the particle distribution f is given as a population of the lattice direction i, and the time step is Δt. S_i is the Guo-forcing term (Guo et al., 2002)

$$S_i = \left(1 - \frac{\Delta t \omega^+}{2}\right) w_i \left(\frac{\boldsymbol{c}_i - \boldsymbol{u}}{c_s^2} + \frac{(\boldsymbol{c}_i \boldsymbol{u})\boldsymbol{c}_i}{c_s^4}\right) \cdot \boldsymbol{f} \tag{3}$$

with the lattice speed of sound $c_s = \frac{\Delta x}{\sqrt{3}\Delta t}$, the lattice spacing Δx, the fluid velocity $\boldsymbol{u}$, and the force density $\boldsymbol{f}$. All simulations are run in 2D; thus, the discrete lattice vectors for a D2Q9 lattice

$$\boldsymbol{c}_i = \left\{ \begin{pmatrix}0\\0\end{pmatrix}, \begin{pmatrix}1\\0\end{pmatrix}, \begin{pmatrix}-1\\0\end{pmatrix}, \begin{pmatrix}0\\1\end{pmatrix}, \begin{pmatrix}0\\-1\end{pmatrix}, \begin{pmatrix}1\\1\end{pmatrix}, \begin{pmatrix}-1\\1\end{pmatrix}, \begin{pmatrix}1\\-1\end{pmatrix}, \begin{pmatrix}-1\\-1\end{pmatrix} \right\} \tag{4}$$

are used. The lattice weights are defined as

$$w_i = \left\{ \frac{4}{9}, \frac{1}{9}, \frac{1}{9}, \frac{1}{9}, \frac{1}{9}, \frac{1}{36}, \frac{1}{36}, \frac{1}{36}, \frac{1}{36} \right\}. \tag{5}$$

However, we note that the method described here is not restricted to 2D; our implementation can easily be extended to 3D. The lattice Boltzmann method solves the macroscopic Navier-Stokes equations with the kinematic viscosity (Krüger et al., 2017)

$$\nu = c_s^2 \left(\frac{1}{\omega^+} - \frac{1}{2}\right) \frac{\Delta x^2}{\Delta t}. \tag{6}$$

The choice for ω^- is not physically motivated, but rather a numerical choice. Typically for TRT simulations, one chooses a magic parameter Λ, which is a well-known parameter in the lattice Boltzmann community that optimizes stability or order of accuracy. In the following, $\Lambda = \frac{3}{16}$ is used, which is the choice to optimize the accuracy of the no-slip plane of the boundaries (Krüger et al., 2017). In the two-phase setup, the viscosity in the liquid and gas phases can be set independently. For simplicity and the demonstration of the algorithm, we restrict ourselves to the case of equal viscosity in liquid and gas phases $\nu = \nu_l = \nu_v$, which is an oversimplification for realistic systems but is generally not a restriction of the algorithm. Because flow in porous media is investigated, boundary conditions are necessary to describe the solid regions of the porous medium. In this study, all solid grid cells are modeled as bounce-back boundaries, resulting in no-slip conditions at the surface.

2.2 Shan-Chen Pseudopotential Method

The Boltzmann lattice equation described so far is not suitable to describe phase separation (Krüger et al., 2017) due to its ideal gas-like Equation of State (EOS). Therefore, it is necessary to introduce a contribution to the pressure tensor that causes phase

separation. The force can act between the phases of a fluid or between different components of the fluid. An interaction parameter $\eta_{\alpha\beta}$ is introduced, which indicates the strength of the interaction between the components α and β. In the case of phase separation of a single-component liquid, $\alpha = \beta$ and $\eta_{\alpha\beta} = \eta$.

The force density acting between two lattice sites is then adopted as

$$\boldsymbol{f}^{\mathrm{SC}}(\boldsymbol{x}) = -\phi(\rho(\boldsymbol{x}))\eta \sum_i w_i \phi(\boldsymbol{x} + \boldsymbol{c}_i \Delta t)\boldsymbol{c}_i \Delta t, \tag{7}$$

with the pseudopotential function

$$\phi(\rho(\boldsymbol{x})) = \sqrt{\frac{c_s^2 \rho - p_{\mathrm{EOS}}(\rho)}{c_s^2 \Delta t^2}}. \tag{8}$$

This pseudopotential function allows us to enforce an EOS with the prerequisite that the pressure must be a function of the fluid density. The EOS employed here is a modified Carnahan-Starling Equation of State

$$p_{\mathrm{EOS}} = \rho R T \frac{1 + b\rho/4 + (b\rho/4)^2 - (b\rho/4)^3}{(1 - b\rho/4)^3} - a\rho^2. \tag{9}$$

with parameters $a = 0.4963 R^2 T_c^2 / p_c$ and $b = 0.18727 R T_c / p_c$ (Li et al., 2013). The parameters R and b set the coexistence densities of the liquid-vapor system ($b = 4$ and $R = 1$ in simulation units). The parameter a is responsible for the thickness of the interface between the phases (Li et al., 2013). This EOS applies very well to fluids (Ribeiro et al., 2014; Checoni & Aznar, 2014; Liu, 2021; Kupershtokh et al., 2009). The first term on the right-hand side accounts for the non-negligible volume of molecules, and the second term acts as an attractive term between molecules (Chen et al., 2014). This EOS is well suited for simulations with high density ratios, up to 900 for liquid density to gas density (Liu et al., 2016; Li et al., 2016; Yuan & Schaefer, 2006). Other EOS can also be used; two well-known examples are the Peng-Robinson and the Van-der-Waals EOS.

In this work, a modified forcing scheme based on the Guo forcing is used, which is referred to as the Li forcing. Li forcing (Li et al., 2012) assumes a shifted value for the local fluid velocity $\boldsymbol{u}(\boldsymbol{x}, t)$ only in the calculations of the force components $\boldsymbol{f}_i$, such that a better agreement of the mechanical stability condition with the Maxwell construction is achieved. The local fluid velocity then becomes (Li et al., 2012)

$$\boldsymbol{u}^* = \boldsymbol{u} + \frac{\sigma \boldsymbol{f}}{\nu \phi^2}. \tag{10}$$

This modified fluid velocity allows one to adjust the coexistence curve with the σ parameter until it matches the Maxwell construction. The modification introduces the term (Li et al., 2012)

$$P_{ij} = P_{ij,\mathrm{original}} + 2\partial_t \eta^2 \Delta x^4 \sigma \partial_i \phi \partial_j \phi \tag{11}$$

into the macroscopic pressure tensor of the Navier-Stokes equations. This preserves the shape of the pressure tensor and thus leaves the Navier-Stokes equation unchanged (Li et al., 2012). For a temperature of $T = 0.65 T_c$, the density ratio between the vapor phase and the fluid phase is 68. The parameter a is adjusted accordingly so that an interface thickness of $6\Delta x$ is obtained. The resulting coexistence densities are shown in Figure 1, where good agreement can be observed with the densities of the Maxwell construction for a range of temperatures.

2.2.1 Contact Angles

In systems with multiple fluid phases or components, contact angles play an important role, as they are governed by the interactions between each phase. A basic de-

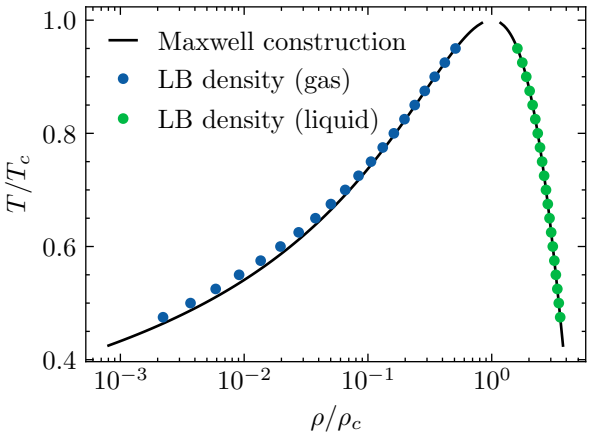

Figure 1. Coexistence densities of the Carnahan-Starling equation of state in a lattice Boltzmann simulation simulated by the Shan-Chen method with the Li-forcing extension. The temperature of the equation of state is plotted against the fluid and vapor densities.

scription is provided by Young's equation, which relates the contact angle at the three-phase contact line (De Gennes, 1985)

$$\cos(\theta_Y) = \frac{\gamma_{\mathrm{SG}} - \gamma_{\mathrm{SL}}}{\gamma_{\mathrm{LG}}} \tag{12}$$

to the surface tensions γ between solid and gas (SG), solid and liquid (SL), and liquid and gas (LG). Experimental studies have shown a correlation between the contact angle and the behavior of evaporation in porous media (Qin et al., 2021; Shokri et al., 2009).

In our simulations, we enforce specific contact angles on surfaces using a virtual density approach. In this method, a virtual density is placed inside wall cells, which interact with adjacent fluid cells through the SC force, given by (Shan & Chen, 1993)

$$\boldsymbol{f}_s(\boldsymbol{x}) = -\eta\phi(\rho(\boldsymbol{x}))\sum_i w_i\phi(\rho_s)s(\boldsymbol{x}+\boldsymbol{c}_i\Delta t)\boldsymbol{c}_i, \tag{13}$$

where the indicator function is defined as

$$s(\boldsymbol{x}) = \begin{cases} 0 & \text{for } \boldsymbol{x} \text{ is a fluid cell} \\ 1 & \text{for } \boldsymbol{x} \text{ is a wall cell} \end{cases}. \tag{14}$$

Here, ρ_s is the virtual density within the wall.

Using a constant density in wall cells can lead to significant artifacts, such as the formation of a mass transfer layer (Li et al., 2019). To address this, various improvements have been proposed. A common refinement in Shan-Chen-type models is to calculate ρ as a weighted average of the densities of adjacent fluid cells (Li et al., 2019; Coelho et al., 2021; Huang et al., 2022; Peng et al., 2021). This average is defined as

$$\rho_{\mathrm{average}}(\boldsymbol{x}) = \frac{\sum_i \bar{s}(\boldsymbol{x}+\boldsymbol{c}_i\Delta t)w_i\rho(\boldsymbol{x}+\boldsymbol{c}_i\Delta t)}{\sum_i w_i\bar{s}(\boldsymbol{x}+\boldsymbol{c}_i\Delta t)}, \tag{15}$$

with the inverted indicator function

$$\bar{s}(\boldsymbol{x}) = 1 - s(\boldsymbol{x}) \tag{16}$$

This method significantly reduces boundary artifacts while retaining tunable fluid–solid interactions.

We extend this approach by introducing a linear interpolation term, ensuring that density offsets are applied only at phase interfaces. The final expression for the virtual wall density is

$$\rho_s(\boldsymbol{x}) = \rho_{\text{average}}(\boldsymbol{x}) + \Delta\psi \left(\Delta\rho + \frac{|\rho_{\text{average}}(\boldsymbol{x}) - \bar{\rho}|}{\psi_0} \right), \tag{17}$$

where $\Delta\psi$ is a dimensionless density offset factor controlling the wetting behavior, $\Delta\rho$ is the density difference between the bulk values of the liquid and vapor phases, $\bar{\rho}$ is the average density between the bulk liquid and bulk vapor phases, and ψ_0 is a dimensionless scaling factor that defines the fraction of the liquid-vapor density range that contributes to the interface. In this study, we use a fixed value of $\psi_0 = 0.95$. The average fluid density for each surface cell is calculated using Equation 15.

2.3 Advection-Diffusion

Dissolved species are transported within the fluid through a combination of advection and diffusion. This behavior is governed by the conservation of species concentration, commonly known as the advection-diffusion equation:

$$\partial_t n(\boldsymbol{x}, t) = -\nabla \cdot \boldsymbol{j}(\boldsymbol{x}, t) = D\nabla^2 n(\boldsymbol{x}, t) - \nabla \cdot (n(\boldsymbol{x}, t)\boldsymbol{u}(\boldsymbol{x}, t)) \tag{18}$$

where n denotes the particle concentration and D is a constant diffusion coefficient.

The concentration flux $\boldsymbol{j}$ consists of two contributions: diffusion and advection.

$$\boldsymbol{j}(\boldsymbol{x}, t) = \boldsymbol{j}_{\text{diff}}(\boldsymbol{x}, t) + \boldsymbol{j}_{\text{adv}}(\boldsymbol{x}, t). \tag{19}$$

The first term, diffusive transport, arises from concentration gradients in the fluid. According to Fick's law (Rice & Do, 2006), it is given by:

$$\boldsymbol{j}_{\text{diff}}(\boldsymbol{x}, t) = -D\nabla n(\boldsymbol{x}, t). \tag{20}$$

This formulation assumes an isotropic diffusion coefficient D.

The second term, advective transport, describes the movement of species carried by the flow of the fluid:

$$\boldsymbol{j}_{\text{adv}}(\boldsymbol{x}, t) = \boldsymbol{u}(\boldsymbol{x}, t)n(\boldsymbol{x}, t). \tag{21}$$

This description is valid because the fluid dynamics occur on time scales much longer than those associated with the ballistic motion of the particles, making particle inertia negligible.

2.3.1 Discretization

To numerically solve the advection-diffusion equations, we employ a finite volume discretization on the same grid used for the fluid dynamics governed by the LBM, following the approach of (Rempfer et al., 2016; Capuani et al., 2004).

A central concept of this discretization is the conservation of concentration, as expressed in Equation 19. This can be derived by integrating the equation over an arbitrary control volume V, yielding:

$$\partial_t \int_V n(\boldsymbol{x}, t)\, \mathrm{d}V = -\int_V \nabla \cdot \boldsymbol{j}(\boldsymbol{x}, t)\, \mathrm{d}V. \tag{22}$$

The right-hand side contains the divergence of the flux $\boldsymbol{j}$, which, by Gauss's divergence theorem, can be rewritten as a surface integral:

$$\partial_t \int_V n(\boldsymbol{x}, t)\, \mathrm{d}V = -\int_{\partial V} \boldsymbol{j}(\boldsymbol{x}, t) \cdot \mathrm{d}\boldsymbol{A}. \tag{23}$$

This expression captures the intuitive result that the change in concentration within a volume is determined solely by the net flux across its boundary.

This principle forms the basis of the discretization: fluxes are evaluated at the interfaces between neighboring cells. We consider a regular cubic lattice with uniform cell volume V. Concentrations are defined at grid points located at the centers of the cells, while fluxes are computed at the midpoints between adjacent cells, corresponding to the shared cell surfaces. A schematic of this geometry is shown in Figure 2a).

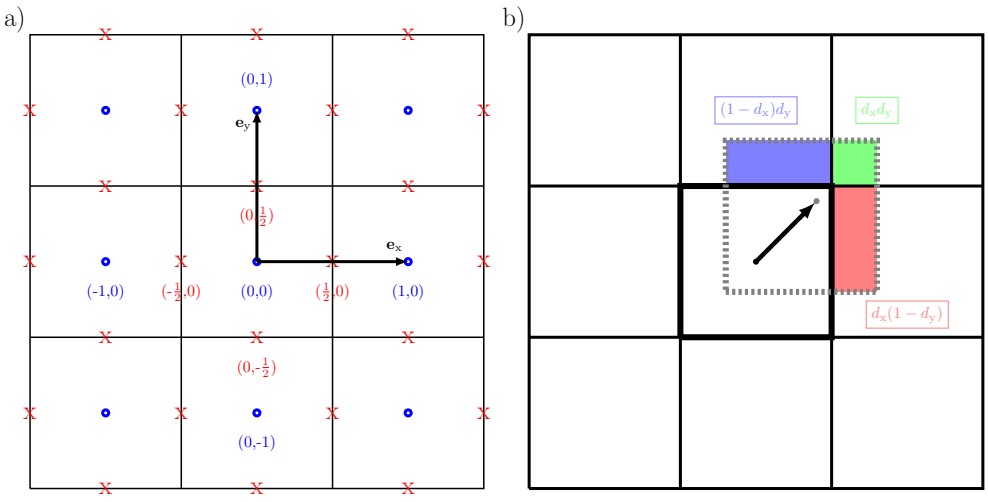

Figure 2. Graphical representations of the discretization schemes. a) Shows the grid points and the evaluation points for the fluxes used in the finite volume method to solve the advection-diffusion equation in 2D. The particle concentrations n are defined on the grid points, which are represented by blue circles. The concentration fluxes $\boldsymbol{j}$ are defined only on the surface of the volume surrounding a grid point, represented by red crosses. The Cartesian lattice vectors $\mathbf{e}_\mathrm{i}$ are also drawn. b) Shows a sketch of the discretization of the advective fluxes in 2D. The central cell is virtually displaced by the fluid velocity $\boldsymbol{u}$ in one time unit $(d_x, d_y) = \boldsymbol{u}\Delta t$. From the overlaps, shown by the different colors, the corresponding fractions of the total concentration contribute to the flux to the cell. The 3D case works analogously.

In technical terms, each cell in 2D has 8 flux directions, and 26 in 3D (Rempfer et al., 2016). Due to the symmetry of the lattice and conservation of concentration, only half of the fluxes need to be stored: the outgoing flux from one cell is equal in magnitude and opposite in sign to the incoming flux of its neighbor.

Discretizing the integral from Equation 23 using a step size Δt, we obtain:

$$\frac{\bar{n}(\boldsymbol{x}, t+\Delta t) - \bar{n}(\boldsymbol{x}, t)}{\Delta t} = -\sum_i \boldsymbol{A}_i \cdot \boldsymbol{j}(\boldsymbol{x} + \frac{\boldsymbol{c}_i \Delta t}{2}, t), \tag{24}$$

where $\bar{n}$ is the particle number per cell, and $\boldsymbol{A}_i$ denotes the area element normal to the lattice vector $\boldsymbol{c}_i$. The specific values of $\boldsymbol{A}_i$ depend on the chosen stencil (Kuron et al., 2016).

Assuming a sufficiently large lattice resolution, we can express the particle numbers per cell as:

$$\bar{n} = nV = n\Delta x^3, \tag{25}$$

where V is the volume and Δx the side length of a cubic cell.

Substituting this into Equation 24, we arrive at the discretized evolution equation:

$$n(\boldsymbol{x}, t+\Delta t) = n(\boldsymbol{x}, t) - \frac{\Delta t}{\Delta x^3} \sum_i \boldsymbol{A}_i \cdot \boldsymbol{j}(\boldsymbol{x} + \frac{\boldsymbol{c}_i \Delta t}{2}, t). \tag{26}$$

As mentioned above, the fluxes must be evaluated at the cell faces, while the fields are defined at the cell centers. To address this, we employ interpolation schemes to approximate the required quantities. For scalar fields such as concentration n, linear interpolation yields

$$n(\boldsymbol{x} + \frac{\boldsymbol{c}_i \Delta t}{2}) \quad = \tfrac{n(\boldsymbol{x}+\boldsymbol{c}_i\Delta t)+n(\boldsymbol{x})}{2} \tag{27a}$$

$$\nabla n(\boldsymbol{x} + \frac{\boldsymbol{c}_i \Delta t}{2}) \quad = \tfrac{n(\boldsymbol{x}+\boldsymbol{c}_i\Delta t)-n(\boldsymbol{x})}{|\boldsymbol{c}_i\Delta t|^2} \boldsymbol{c}_i \Delta t. \tag{27b}$$

With this discretization, the diffusive flux from Equation 20 can be written on the lattice as

$$\boldsymbol{j}_{\text{diff}} \left(\boldsymbol{x} + \frac{\boldsymbol{c}_i \Delta t}{2}, t \right) = D \frac{n(\boldsymbol{x} + \boldsymbol{c}_i \Delta t) - n(\boldsymbol{x})}{|\boldsymbol{c}_i \Delta t|^2} \boldsymbol{c}_i \Delta t. \tag{28}$$

This interpolation-based discretization is applied exclusively to the diffusive contribution. For advection, we employ a different scheme, often referred to as the volume-of-fluid method, following Capuani et al. (2004); Rempfer et al. (2016). In this approach, the volume of each cell is virtually displaced over one time step according to the local fluid velocity. The resulting overlaps with neighboring cells determine the magnitude of the advective fluxes. A schematic of the procedure is shown in Figure 2b).

Dimensionless displacements are defined as

$$d_j = \boldsymbol{u} \cdot \mathbf{e}_j \frac{\Delta t}{\Delta x} \tag{29}$$

where $\mathbf{e}_j$ are the Cartesian unit vectors. The corresponding advective fluxes are given by

$$\boldsymbol{j}_{\text{adv}}(\boldsymbol{x} \pm \frac{\mathbf{e}_x}{2}, t) = n(\boldsymbol{x}, t) d_x (1 - d_y) \mathbf{e}_x \frac{\Delta x}{\Delta t} \begin{cases} 1 & \text{if } d_x \lesseqgtr 0 \\ 0 & \text{otherwise} \end{cases} \tag{30a}$$

$$\boldsymbol{j}_{\text{adv}}(\boldsymbol{x} \pm \frac{\mathbf{e}_y}{2}, t) = n(\boldsymbol{x}, t) d_y (1 - d_x) \mathbf{e}_y \frac{\Delta x}{\Delta t} \begin{cases} 1 & \text{if} d_y \lesseqgtr 0 \\ 0 & \text{otherwise} \end{cases} \tag{30b}$$

$$\boldsymbol{j}_{\text{adv}}(\boldsymbol{x} + \frac{\mathbf{e}_x}{2} \pm \frac{\mathbf{e}_y}{2}, t) = n(\boldsymbol{x}, t) |d_x d_y| \frac{\mathbf{e}_x \pm \mathbf{e}_y}{\sqrt{2}} \frac{\Delta x}{\Delta t} \begin{cases} 1 & \text{if } d_x > 0 \wedge d_y \lesseqgtr 0 \\ 0 & \text{otherwise} \end{cases} \tag{30c}$$

$$\boldsymbol{j}_{\text{adv}}(\boldsymbol{x} - \frac{\mathbf{e}_x}{2} \pm \frac{\mathbf{e}_y}{2}, t) = n(\boldsymbol{x}, t) |d_x d_y| \frac{-\mathbf{e}_x \pm \mathbf{e}_y}{\sqrt{2}} \frac{\Delta x}{\Delta t} \begin{cases} 1 & \text{if } d_x < 0 \wedge d_y \lesseqgtr 0 \\ 0 & \text{otherwise} \end{cases}. \tag{30d}$$

2.4 Precipitation

The advection-diffusion equation describes the movement of dissolved species in the fluid. However, if the concentration of species in the fluid becomes too high, precipitation can occur. To capture this effect in a continuum description, the model must be extended. We here propose to include crystallization in a continuum framework in terms of a chemical reaction.

We consider precipitation to occur above a threshold concentration, called the saturation concentration n_{sat}. If the concentration in the fluid phase surpasses this threshold, precipitates will form on surfaces present in the system. In our model, these surfaces

accumulate the concentration until a critical amount is reached, called the crystal concentration n_{crystal}. At that point, the cell crystallizes and its neighboring cells continue the same process, promoting crystal growth.

Spontaneous crystal formation in the bulk fluid is excluded, as the concentrations used are well below the limit at which homogeneous precipitation occurs (Desarnaud et al., 2014). A representation of our model process is shown in Figure 3.

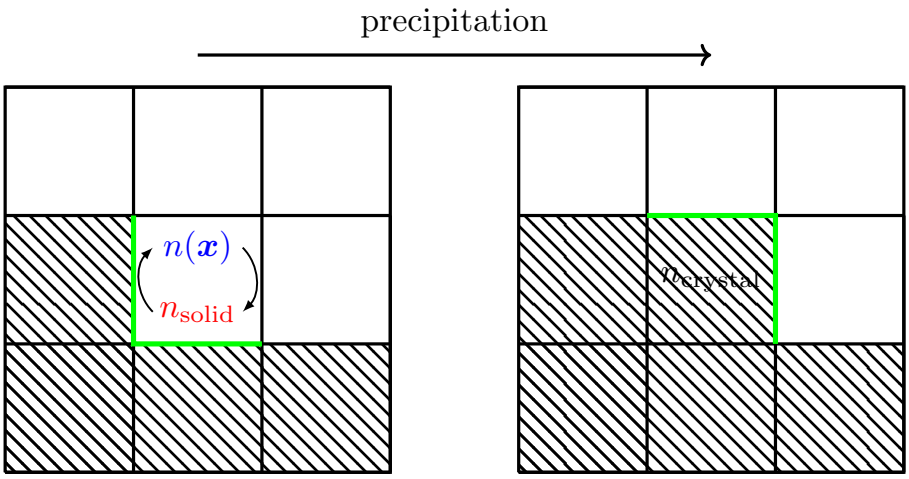

Figure 3. The process of precipitation in a fluid cell. White cells represent fluid regions, while shaded cells indicate solid regions. The concentration of the species n in a fluid cell is converted into solid concentration n_{solid} at the active surfaces, which are highlighted in green. After the solid concentration reaches the crystal concentration n_{crystal}, the cell becomes a solid crystal, and its surfaces become active for further crystal growth.

Chemically, dissolution and precipitation occur only at the liquid-solid interface and can be described as an equilibrium reaction of species S (Chen et al., 2013):

$$S_{\text{aq}} \rightleftarrows S_{\text{solid}} \tag{31}$$

representing the exchange between the dissolved and solid phases of the species.

The boundary condition at the interface is given by the following:

$$D\nabla n = k\left(n_{\text{aq}} - n_{\text{sat}}\right)\mathbf{q}, \tag{32}$$

where n_{aq} is the concentration in the fluid cell, n_{sat} is the saturation concentration, $\mathbf{q}$ is the surface normal, and k is the reaction rate (Chen et al., 2013, 2015). For our simulations, this rate is taken to be constant, although it is generally temperature-dependent.

In practice, this means that the accumulated concentration can be described by the flux through active surfaces, as given by the right-hand side of Equation 32. This flux is defined as follows:

$$\boldsymbol{j}_{\text{precip}} = k\left(n_{\text{aq}} - n_{\text{sat}}\right)\mathbf{q}. \tag{33}$$

The change in concentration over time can then be obtained by integrating the flux over the active surface area O in the local environment:

$$\frac{\mathrm{d}\bar{n}}{\mathrm{d}t} = \int_O \boldsymbol{j}_{\text{precip}}\,\mathrm{d}\mathbf{A}. \tag{34}$$

This leads to the following rate equation that describes the reaction kinetics:

$$-\frac{\mathrm{d}\bar{n}_{\mathrm{solid}}}{\mathrm{d}t} = \frac{\mathrm{d}\bar{n}_{\mathrm{aq}}}{\mathrm{d}t} = -Ok\left(n_{\mathrm{aq}} - n_{\mathrm{sat}}\right). \tag{35}$$

Consequently, the amount of precipitated species n_{solid} or dissolved species n_{aq} is proportional to supersaturation, defined as the concentration above the saturation concentration n_{sat}.

2.4.1 Implementation as a Boundary Condition

The chemical reaction model presented for precipitation can be implemented as a boundary condition for the concentration field in the system.

If a fluid cell containing liquid neighbors a solid surface and the concentration of the species exceeds the saturation concentration, precipitation occurs on the solid surface. Because each active surface contributes to the accumulation, a larger number of active surfaces leads to increased precipitation and, consequently, faster crystallization of the cell. Precipitation does not immediately accumulate enough material to crystallize a cell, which requires storing the accumulated concentration in each cell. This accumulated amount is called n_{solid}.

The total change in concentration is then given by the following:

$$\Delta n_{\mathrm{aq}} \quad = |\boldsymbol{j}_{\mathrm{precip}}| \sum_i A_i^* \Delta t \tag{36a}$$

$$\Delta n_{\mathrm{solid}} \quad = -|\boldsymbol{j}_{\mathrm{precip}}| \sum_i A_i^* \Delta t, \tag{36b}$$

where A_i^* are the active surface areas.

This implementation allows species to flow across the cell boundaries, meaning that the cell behaves like a gradually growing or dissolving crystal. When the accumulated solid concentration reaches the cell-filling crystal concentration n_{crystal}, the cell is converted into a no-slip cell for the fluid and a no-flux cell for the species, thus stopping all local dynamics. At this point, the surfaces of the newly crystallized cell are also marked as active surfaces to enable further growth.

Due to the use of a fixed timestep, excess concentration beyond the threshold n_{crystal} may accumulate in the crystallizing cell. To conserve total species concentration in the system, this excess is redistributed uniformly among all fluid-phase cells. This approximation is valid when crystal growth is gradual and species are expected to have already equilibrated throughout the domain during the growth process (Chen et al., 2013).

2.5 Coupling with the Fluid

The coupling between the fluid and the dissolved species arises from two main mechanisms: frictional interaction due to relative motion (Rempfer et al., 2016), and preferential solubility of the species in different phases (Rivas et al., 2018; Rotenberg et al., 2010).

The frictional coupling is described by the following equation:

$$\boldsymbol{f}(\boldsymbol{x}, t) = \frac{k_{\mathrm{B}}T}{D}\boldsymbol{j}_{\mathrm{diff}}(\boldsymbol{x}, t), \tag{37}$$

which represents a force proportional to the diffusive flux, and thus to the relative velocity between the fluid and the dissolved species (Rempfer et al., 2016).

The second contribution stems from preferential solubility, quantified by the solvation energies of the species in the respective bulk phases. The difference in solvation energy is known as the Gibbs transfer energy, defined as:

$$\Delta\mu = \mu^{\mathrm{l}}_{\mathrm{solvation}} - \mu^{\mathrm{g}}_{\mathrm{solvation}}. \tag{38}$$

This quantity characterizes the energy change associated with the transfer of a species particle from the gas phase (g) to the liquid phase (l). It is a property of the species-fluid pair and is an input parameter in the model. The Gibbs transfer energy governs the equilibrium partitioning of the species, typically resulting in concentrations much higher in the liquid phase than in the gas phase.

Applying the Gibbs-Duhem relation for isothermal systems ($dT = 0$), the resulting gradients in chemical potential translate into forces that are incorporated into the system's dynamics:

$$\boldsymbol{f}(\boldsymbol{x}, t) = -\nabla p(\boldsymbol{x}, t) = -\frac{N}{V}\nabla\mu(\boldsymbol{x}, t). \tag{39}$$

Note the spatial dependence of the chemical potential, which also applies to the solvation chemical potential. Since solvation potentials are defined only in bulk phases, a model is needed to interpolate their values at the phase interface. A simple and effective choice is to use the density of the fluid as an indicator of the interpolation between the bulk values (Rivas et al., 2018):

$$\mu_{\mathrm{sol}}(\boldsymbol{x}, t) = \frac{\Delta\mu}{\Delta\rho}\rho(\boldsymbol{x}, t), \tag{40}$$

where $\Delta\rho$ denotes the difference in fluid densities between the bulk phases.

By combining Equation 39 and Equation 40, we obtain an additional contribution to the diffusive flux:

$$\boldsymbol{j}_{\mathrm{sol}}(\boldsymbol{x}, t) = -\frac{D}{k_{\mathrm{B}}T}n(\boldsymbol{x}, t)\frac{\Delta\mu}{\Delta\rho}\nabla\rho(\boldsymbol{x}, t). \tag{41}$$

As discussed earlier, this additional flux also contributes to the frictional coupling.

So far, we have considered only the force that acts on the dissolved species. However, the coupling is reciprocal: It also induces the force on the fluid

$$\boldsymbol{f}(\boldsymbol{x}, t) = -\rho(\boldsymbol{x}, t)\frac{\Delta\mu}{\Delta\rho}\nabla n(\boldsymbol{x}, t), \tag{42}$$

which is applied directly to the fluid.

3 Model Verification

3.1 Contact Angles

The wetting properties of fluids significantly affect the evaporation processes in porous media (Qin et al., 2021; Nguyen et al., 2012; Shokri et al., 2009). Consequently, we examine the model proposed in Section 2.2.1 to determine the relationship between phase field offset and contact angle. To achieve this, we consider droplets positioned on a flat surface. The contact angle of a spherical droplet on a flat wall can be determined by employing basic geometric identities to establish the relationship between the droplet's width, height, radius, and contact angle:

$$\theta = \pi - \arctan\left(\frac{b/2}{r - h}\right). \tag{43}$$

In this context, b represents the width of the droplet on the wall, h denotes the height of the droplet from the wall, and r is the radius of the droplet. A sketch of these quantities is shown in the inset of Figure 4.

The surface defined by $\psi = 0$ is determined numerically. These points are then fitted with a circle, which allows a straightforward determination of the contact angle.

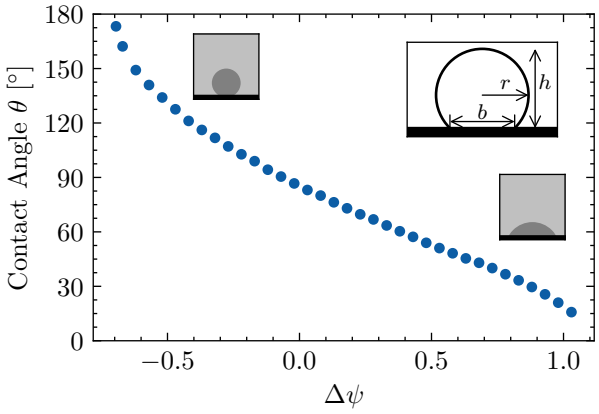

Figure 4. Measured contact angles on a planar surface for different density offset factors $\Delta\psi$. Two insets show representative simulations.

The results of the simulations are shown in Figure 4. A nonlinear relationship is observed between the density offset factor $\Delta\psi$ and the contact angle. For values of $\Delta\psi \leq -0.68$, the droplet detaches from the wall. In contrast, the droplet completely wets the surface for $\Delta\psi \geq 1.1$.

3.2 Salt Crystal Growth

To validate the accuracy of the precipitation algorithm, a cylindrical crystal is initialized in a cylindrical domain. Its radius is set to $R = 128\Delta x$, and the boundary of the domain is maintained at a constant concentration of $n_0 = 1.5 n_{\text{sat}}$.

Such a radially growing crystal can also be analyzed analytically. Assuming quasi-steady-state growth, one can derive (Rice & Do, 2006):

$$\frac{\mathrm{d}R}{\mathrm{d}t} = \frac{D(n^* - n_0)}{n_{\text{crystal}} R \ln(\frac{R}{R_1})}, \tag{44}$$

where R is the crystal radius, R_1 is the distance to the concentration boundary, and n^* is the concentration at the crystal surface.

The reaction constant $k = 23.4\,\mu\text{m}\,\text{s}^{-1}$ (Naillon et al., 2017), molar volume $v_m = 26.93\,\text{cm}^3\,\text{mol}^{-1}$, diffusion coefficient $D = 1.3{\times}10^{-9}\,\text{m}^2\,\text{s}^{-1}$ (Naillon et al., 2017), saturation concentration $n_{\text{sat}} = 6.16\,\text{mol}\,\text{L}^{-1}$ (Zimmermann et al., 2015) and the crystal concentration $n_{\text{crystal}} = 0.026\,93\,\text{cm}^3\,\text{mol}^{-1}$ are chosen to match NaCl.

An example of simulated crystal growth is shown in Figure 5. Figure 5a) shows snapshots of the crystal growth for the first few seconds of the simulation. In Figure 5b) the radial growth is shown quantitatively by plotting the crystal radius above a dimensionless simulation time τ_D and the corresponding analytic solution.

There is good agreement between the simulation and the analytical solution. However, for longer simulation times, lattice artifacts appear, resulting in slightly non-cylindrical growth. These artifacts are more pronounced for higher reaction rates k and lead to larger deviations from the analytical prediction. However, in the early stages of growth, the crystal remains cylindrically symmetric.

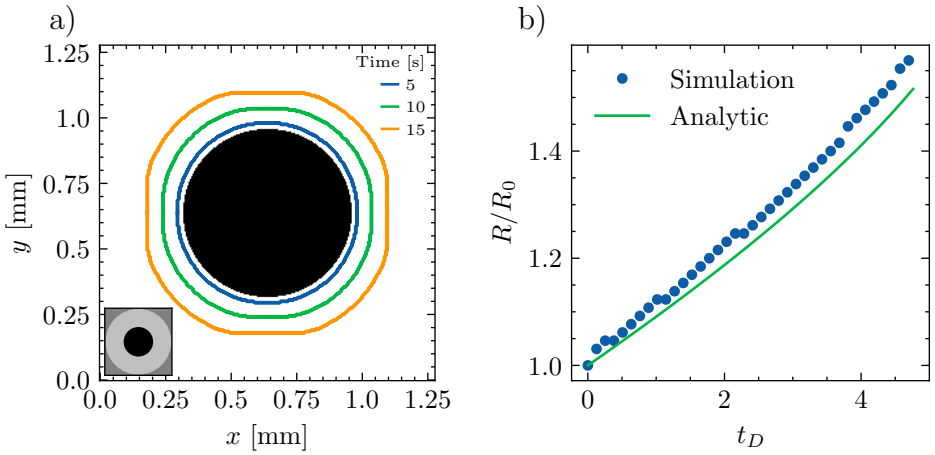

Figure 5. a) Temporal growth of a cylindrical crystal, shown in solid black. The surface contour of the crystal is depicted at various growth stages. The inset shows the simulation setup: the light gray area is the domain, and the dark gray region indicates the concentration boundary condition. b) Salt crystal growth from a cylindrical nucleus over time in a simulation with a constant concentration boundary condition. Radii are plotted against the dimensionless diffusion time $t_D = tD/R_0^2$.

3.3 Evaporation Measurement

To model evaporation in the system, a pressure boundary condition is applied at the top of the simulation domain in the vapor phase (Hessling et al., 2017). Its value is set slightly below the equilibrium pressure, inducing evaporation of the liquid phase. Vapor is removed at the boundary and replenished by liquid evaporating from the interface.

However, the resulting evaporation rates cannot be predicted analytically and must be measured directly in simulation. A series of simulations with a planar liquid-vapor interface at various pressure boundary values is used to determine these rates, shown in Figure 6.

Interpolating between the measured values allows us to select the desired evaporation rate for specific simulations. As evaporation proceeds, the liquid volume decreases, leading to an increasing concentration of the dissolved species, eventually resulting in precipitation.

4 Results

4.1 Salt Precipitation in a Porous Medium

With the model verified, we apply it to a more complex problem: salt precipitation in a 2D porous medium. We investigate saturation curves and their dependence on wetting, where saturation S is the fraction of the accessible volume filled with fluid. For our simulation domain, we use a 2D system containing an array of square pollers on a regular grid with a poller width of $16\Delta x$ and a poller spacing of $16\Delta x$, resulting in a domain size of (258, 462) lattice sites. In the horizontal direction, periodic boundary conditions are employed and in the vertical direction the fluid is evaporated. A snapshot of the geometry is shown in Figure 7.

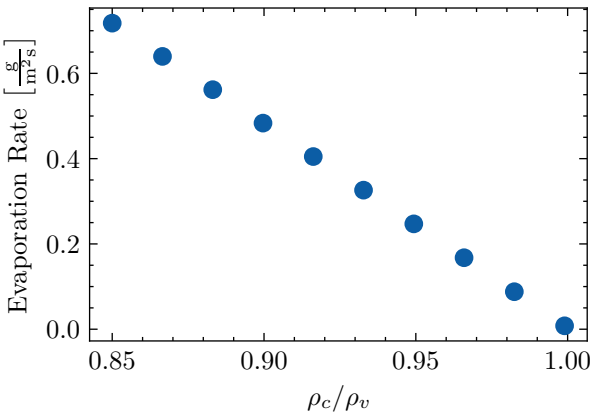

Figure 6. Evaporation rate through a planar, infinite liquid–vapor interface. The rate is plotted against the density value enforced at the pressure boundary condition, given in units of the vapor density.

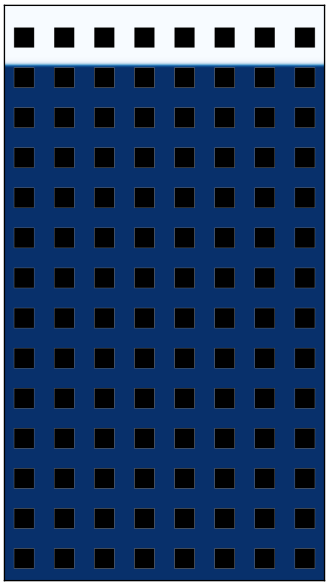

Figure 7. Porous geometry used in the simulations with an initial filling height of 90 % for a neutral wetting case. The liquid phase is shown in blue, the vapor phase in white and the solid pollers of the porous medium in black. Periodic boundary conditions are employed in the horizontal direction, and the fluid is evaporating in the vertical direction from the bottom to the top.

Initially, the geometry is filled up to a filling height of 90 %. These fluid cells are also filled with the dissolved species at saturation concentration n_{sat}, and the system is then equilibrated before evaporation is switched on. In all systems, gravity is neglected, which corresponds to an experimental setup where the fluid cell is placed horizontally and the evaporation is controlled by dry air flowing at the top of the domain.

Then these systems are investigated for the varying contact angles θ_{wall} between the porous geometry and the fluid. The simulation is performed at $T = 0.85\,T_c$, with a diffusion coefficient $D = 0.02\,\frac{\Delta x^2}{\Delta t}$, a Gibbs transfer energy of $\Delta\mu = \frac{10}{3}\,k_{\text{B}}T$, a saturation concentration of $n_{\text{sat}} = 0.0037\,\frac{1}{\Delta x^3}$, a crystal concentration of $n_{\text{crystal}} \approx 6n_{\text{sat}}$ and a reaction rate of $k = 0.0244\,\frac{\Delta x}{\Delta t}$. The parameters were chosen to mimic the precipitation of sodium chloride in water, but with a reduced solubility, corresponding to lower density, to improve numerical stability. However, all relevant parameters regarding precipitation are matched. The evaporation boundary condition is set to $\rho_c = 0.875\rho_v$, which according to Figure 6 corresonds to an evaporation rate of $\approx 0.6\,\text{g}\,\text{m}^{-2}\,\text{s}^{-1}$. The wetting properties between the fluid and the porous geometry θ_{wall} and between the fluid and the forming salt crystals θ_{salt} can be tuned independently.

4.1.1 Wetting, Neutral and Non-Wetting Behaviour

During evaporation in porous media, the interface between fluid and vapor temporarily sticks to pores with a small width. This phenomenon also appears during imbibition/drainage and is commonly referred to as Haines jumps (Sun & Santamarina, 2019). The pressure difference between the wetting phase p_w and the non-wetting phase p_n at the interface of the pores is given by

$$\Delta p(\boldsymbol{x}) = -\frac{2\gamma\cos(\theta - \alpha(\boldsymbol{x}))}{d(\boldsymbol{x})}, \tag{45}$$

where γ is the surface tension, θ is the contact angle, $\alpha(\boldsymbol{x})$ is the local angle between the pore wall and the flow direction and $d(\boldsymbol{x})$ is the width of the pore.

The mechanism behind the Haines jumps can be explained by assuming a fixed pressure difference over a porous medium filled with a fixed amount of liquid. The interface will move to a narrow pore throat and balance the prescribed pressure difference by curving its interface. This occurs because it allows for the minimum area for the liquid-gas interface while also obeying the prescribed contact angle. This is a local energy minimum; small changes in the pressure difference will only slightly change the overall position of the interface until the geometry does not allow for further compensation. Then the position will jump to another pore throat, allowing for the expected pressure difference.

First, we run reference simulations in the absence of salt and measure the saturation of the porous medium for various wettabilities. After an initial equilibration of the saturated porous medium, evaporation is switched on. These serve as a baseline and are shown as solid lines in Figure 8.

One can observe that with only evaporation considered, larger contact angles lead to faster evaporation, resulting in a more rapid drop in the saturation curves, until all fluid has evaporated from the porous medium. This can be explained by the pressure differences between the liquid, the gas, and the boundary condition used for evaporation. In the case of high wettability, the interface is curved away from the gas phase, which means that the pressure in the gas phase is increased by the Laplace pressure through the interface. Inversely, for low wettability, the curvature flips and the pressure in the gas phase is decreased. In both cases, the evaporation boundary condition is the same, leading to the same pressure at the outlet. Since the pressure at the interface increases in one case and decreases in the other, the pressure difference from the interface to the evaporation boundary condition, driving the mass transport out of the system, follows

that trend. Higher pressures at the interface, which occur for higher contact angles, lead to faster evaporation and vice versa.

4.1.2 Precipitation Clogging

Next, we investigate the influence of precipitation on the saturation curves, for the cases where the wettability of the salt crystals is equal to that of the porous medium ($\theta_{\text{porous}} = \theta_{\text{salt}} = \theta$). The resulting evaporation curves are shown as dashed lines in Figure 8.

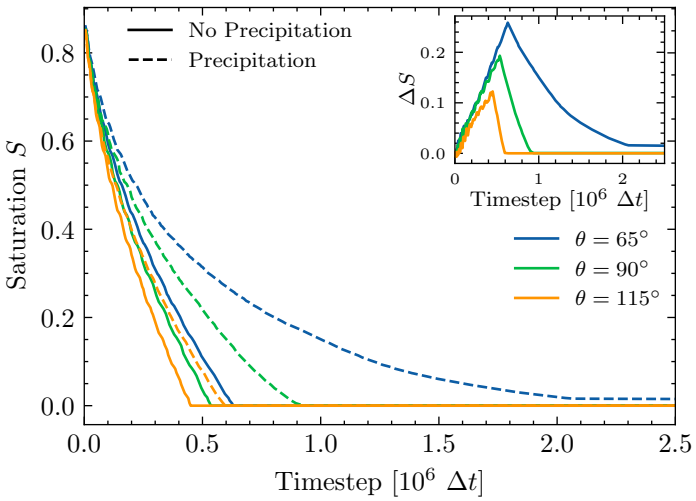

Figure 8. Saturation curves of the porous medium for different wettabilities for the pure evaporation case (solid) compared to the case of salt precipitation (dashed), which has equal wetting for the porous medium and the precipitated salt. The saturation is defined as the fraction of accessible volume filled with fluid. For a better comparison, the differences in saturation ΔS are shown for each of the wettabilities as an inset, demonstrating that smaller contact angles lead to slower evaporation. A video of the evaporation process can be seen in (Reinauer et al., 2025) (`saturation_equal_wetting.mp4`).

As expected, precipitation in the porous medium leads to a decreased evaporation rate, which results in slower drying of the porous medium because these simulations are performed in the diffusion-limited regime. To better highlight the differences between the investigated wettabilities, the inset of Figure 8 shows the saturation differences between the simulations, including precipitation and pure evaporation for fixed wettability $\Delta S = S_{\text{precip}} - S_{\text{evap}}$. We can observe a common slowdown for all wettabilities attributed to the narrowing of the pores as a result of the initial crystallization of the salt at the beginning of evaporation. This can also be observed in the crystal fraction over saturation in Figure 9a), where the crystal fraction is defined as the volume occupied by the crystal compared to the overall accessible volume, analogous to the saturation of the fluid.

After the initial crystallization, the crystal fraction slowly begins to separate for the different wettabilities, where the largest number of salt crystals is formed for the smallest contact angle, which, also shows the largest slowdown of evaporation in Figure 8. However, a large influence on the evaporation process is not primarily due to the amount of salt precipitated, but rather due to the locations where the salt crystals form in the porous medium. For smaller contact angles, crystals are preferably formed at the entrances of the pores, thus increasing the probability of pores clogging, while for larger contact an-

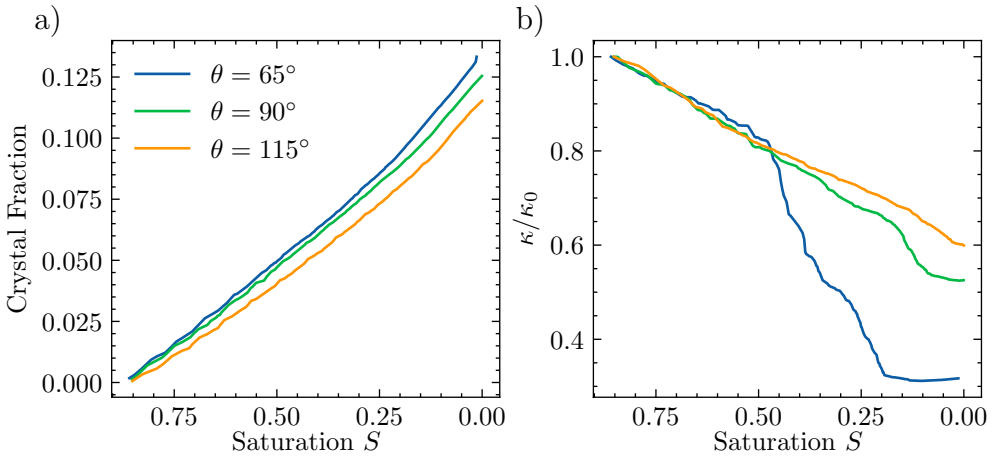

Figure 9. a) Fraction of the precipitated salt of the total volume over the saturation S for an equal wetting of the porous medium and the precipitated salt. b) Normalized permeability at different saturation levels in the pore. The precipitated salt is narrowing and clogging the pores, leading to a smaller permeability, resulting in a slower evaporation process.

gles, the salt more rarely completely clogs a channel, mainly only narrowing it (see Figure 10). This clogging naturally leads to slower evaporation of the fluid because diffusion channels through the porous medium are blocked. This leads to an increase in the saturation difference, which increases until the entire fluid has evaporated in the precipitation-free case, leading to characteristic kinks in the saturation difference curves in Figure 8. Quantifying the reason for this slowdown is challenging, as it depends on the complex interplay between the wettability and salt precipitation, which influences the already complex shape of the porous medium, as well as the moving fluid front within the porous medium. A reasonable approximation for the quantification is to neglect the movement of the fluid front and use Darcy's law to quantify the influence of pore clogging on the average fluid velocity through the porous medium (Dullien, 1992; Pan et al., 2001). It reads

$$\kappa = -\frac{\mu \langle \boldsymbol{u} \rangle}{\Delta p}, \tag{46}$$

where κ is the permeability, μ is the dynamic viscosity, Δp is the difference in pressure between inlet and outlet, and $\langle \boldsymbol{u} \rangle$ is the average velocity inside the porous medium. For each geometry during the precipitation process, a separate set of simulations is performed to measure the permeability through the average fluid velocity for a fixed pressure difference between the bottom and top of the medium. The resulting permeabilities at different saturations are shown in Figure 9b), and a qualitative visualization of the system showing the fluid velocities inside the porous medium at a saturation value of 0.1 in Figure 10.

In the permeability curves, the influence of the pores narrowing is observed as a result of the precipitated salt, which is expected to decrease the permeability of the porous medium. In addition, the permeability curves feature distinct drops, which can be attributed to the sealing of distinct pores by the precipitated salt, removing the contribution of these fluid paths to the permeability. This is especially pronounced in the case of the lowest contact angle, where large parts of the domain are sealed off by the salt, resulting in a very sharp drop in the permeability. This sealing can also trap fluid inside the pores, which can be seen by the non-zero saturation values in Figure 8 for the low contact angles. This blocking off can also be seen in the fluid velocity in Figure 10,

Figure 10. Qualitative visualization of the permeability measurements of an exemplary topology from the simulation. For each topology in the evaporation process, the permeability is measured by applying a pressure difference between the top and bottom of the porous medium. The porous medium is shown in black, the precipitated salt is shown in grey, and the magnitude of the velocity is shown in the color code, where blue means slow fluid flow and red means fast fluid flow. Several fluid paths are blocked, which depend on the wettability, while only a few remain unaffected, showing an increase in fluid velocity. A video of the different permeabilities can be seen in (Reinauer et al., 2025) (permeability_equal_wetting.mp4).

Lattice Boltzmann simulations of liquid-gas and binary uid systems. Physical Review E, 54(5), 5041{5052. doi: 10.1103/PhysRevE.54.5041

Swift, M. R., Osborn, W. R., & Yeomans, J. M. (1995, July). Lattice Boltzmann Simulation of Nonideal Fluids. Physical Review Letters, 75(5), 830{833. doi: 10.1103/PhysRevLett.75.830

Tartakovsky, A. M., Meakin, P., Scheibe, T. D., & Wood, B. D. (2007, May). A smoothed particle hydrodynamics model for reactive transport and mineral precipitation in porous and fractured porous media. Water Resources Research, 43(5), 2005WR004770. doi: 10.1029/2005WR004770

Veran-Tissoires, S., & Prat, M. (2014, June). Evaporation of a sodium chloride solution from a saturated porous medium with e orescence formation. Journal of Fluid Mechanics, 749, 701{749. doi: 10.1017/jfm.2014.247

Yang, J., Lei, T., Wang, G., Xu, Q., Chen, J., & Luo, K. H. (2023, October). Lattice Boltzmann modelling of salt precipitation during brine evaporation. Advances in Water Resources, 180, 104542. doi: 10.1016/j.advwatres.2023.104542

Yuan, P., & Schaefer, L. (2006). Equations of State in a Lattice Boltzmann Model. Physics of Fluids, 18(4), 042101. doi: 10.1063/1.2187070

Zimmermann, N. E. R., Vorselaars, B., Quigley, D., & Peters, B. (2015, October). Nucleation of NaCl from Aqueous Solution: Critical Sizes, Ion-Attachment Kinetics, and Rates. Journal of the American Chemical Society, 137(41), 13352{13361. doi: 10.1021/jacs.5b08098